34th Symposium on Naval Hydrodynamics
Washington, D.C., June 26 – July 1, 2022

Quantifying Fragmentation Statistics in Two-Phase Turbulent Flows for Ship Wake Applications

Declan B. Gaylo, Kelli Hendrickson, Dick K.P. Yue
(Massachusetts Institute of Technology, Cambridge, MA USA)

ABSTRACT

The bubbly wake is a prominent and highly observable feature of surface vessels and near-surface submarines; however, modeling the size-distribution of bubbles in the bubbly wake is an outstanding challenge in computational ship hydrodynamics. We recently derived a time scale $\tau_c = C_\tau \varepsilon^{-1/3} {a_{max}}^{2/3}$, where ε is the turbulent dissipation rate and a_{max} the largest bubble injected by entertainment, that separates the complex evolutionary period of the bubble-size distribution from an analytically tractable equilibrium state (Gaylo, *et al.*, 2021) for turbulent bubbly flows dominated by entrainment and strong fragmentation (Weber number $We_P >> 1$). The constant of proportionality C_τ depends on measures of the fragmentation rate of bubbles, the number of daughter bubbles formed from a fragmentation event, and the size distribution of daughter bubbles formed. Unfortunately, their values and the influence of surface tension on these measures remain uncertain. Performing simulations of bubbles fragmenting in isotropic homogeneous turbulence (IHT) at a range of large We_P as an analog of the turbulent bubbly-flow near an entertaining free surface, we use the Eulerian Label Advection method (ELA) (Gaylo, *et al.*, 2022) to track bubbles and provide a complete and robust history of all fragmentation events, including those with more than two daughter bubbles. This history allows us to accurately measure the fragmentation statistics and enables us to calculate $C_\tau \approx 43$. We show that this value is relatively independent of We_P, thus elucidating a critical time scale in the evolution of entraining bubbly wake for computational ship hydrodynamics.

INTRODUCTION

Air entraining flows around a surface vessel or near-surface submarine create a prominent cloud of bubbles in the wake (NDRC, 1946). The larger bubbles in the cloud rise to the surface and create and observable surface slick and the smaller bubbles remain in the wake far behind the vessel (Trevorrow, *et al.*, 1994). Thus, understanding the size distribution of bubbles in the wake is important to the design and operation of naval vessels. A challenge in computational ship hydrodynamics (CSH) is that, due to the many orders of magnitude separating the length and times scales of the bubbles and the length and time scales of the ship, fully resolved simulation of the near-vessel bubbly wake is not feasible (Castro, *et al.*, 2016). A critical area of work to overcome this challenge and accurately predict the near-vessel bubbly wake is understanding the length and times scales involved in each relevant physical mechanism (e.g., entrainment, degassing, fragmentation, coalescence, and dissolution) and their interactions.

Our interest here is how turbulence in the wake influences the number and size distribution of bubbles through entrainment by the interaction of strong turbulence with the free surface, and the fragmentation of larger bubbles into smaller bubbles by turbulence beneath the free surface. On entrainment, recent work has elucidated both the size of bubbles created by turbulent entrainment (Yu, *et al.*, 2020) and the volume (and by extension number) of bubbles entrained (Hendrickson, *et al.*, 2022). Additionally, Yu, *et al.* (2019) showed that during turbulent free-surface entrainment, the flow beneath the free surface is well approximated by isotropic homogeneous turbulence (IHT) following the Kolmogorov energy spectrum.

Using the recent advancements in the understanding of turbulent free-surface entrainment and turbulence near it, we recently performed analysis on the interaction between entrainment and an idealized model of strong fragmentation (Gaylo, *et al.*, 2021). Although the bubble-size distribution initially reflects the size distribution of bubbles injected by entertainment, we found that, for the case of any weak (as defined by the power-law slope of the injected bubble distribution) entrainment, which includes the entrainment model proposed by Yu, *et al.* (2020), fragmentation causes the bubble-size distribution to rapidly evolve to an equilibrium bubble-size distribution. The timescale of this transition is given by

$$\tau_c = (9/2)(\ln m)^{-1}(C_f/C_\Omega)\, \varepsilon^{-1/3}\, {a_{max}}^{2/3} \ , \quad (1)$$

where ε is the turbulent dissipation rate, a_{max} is the largest bubble injected by entertainment, and the rest of the terms are properties of fragmentation: C_Ω relates to

the rate of fragmentation, m is the number of daughter bubbles created by fragmentation, and C_f relates to the size distribution of the daughter bubbles. For times $t < \tau_c$ the bubble-size distribution is dependent on the properties of weak entrainment, but for times $t > \tau_c$ the bubble-size distribution is largely independent of the properties of entrainment, making it analytically tractable. A similar critical time was found by Deike, *et al.* (2016) for breaking waves rather than turbulent entrainment; however, they did not incorporate the effect the size distribution of daughter bubbles, which has been shown to be critical (Qi, *et al.*, 2020).

Through C_Ω, m, and C_f, τ_c depends on the properties of turbulent fragmentation (Gaylo, *et al.*, 2021). There are many models of fragmentation available in literature based on a variety of arguments (Liao & Lucas, 2009); however, these models are not consistent in their predictions of these three values relevant to τ_c. Thus, the application of τ_c to understand the time scales of bubbly-wake simulations is limited by our understanding of fragmentation.

In this work we consider the canonical problem of a cloud of bubbles fragmenting in IHT without gravity or a free surface. The applicability of this canonical problem to describe fragmentation near an entraining free surface was demonstrated by Yu, *et al.* (2019). Eulerian Label Advection (ELA), a tool we recently developed (Gaylo, *et al.*, 2021), provides robust volume-conservative tracking of bubbles and identification of fragmentation, including when more than two daughter bubbles are created. By recording when bubbles fragment and the size of their daughter bubbles, we quantify the properties of fragmentation, C_Ω, m, and C_f, relevant to τ_c. This provides us an accurate measure of the effect of fragmentation on the bubble-size distribution.

FRAGMENTATION MODELING

The bubbles within a flow can be described using the bubble-size distribution $N(a)$, where $N(a)\delta a$ describes the number of bubbles of effective[1] radius $a < a' < a+\delta a$ within domain of interest. The evolution of $N(a)$ can be described by a population-balance equation

$$\frac{\partial N}{\partial t}(a) = S_d(a) + S_f(a) + S_c(a) + I(a) - D(a)\,, \quad (2)$$

where the terms on the right side relate to the five physical mechanisms that acts on the bubbles. Three mechanisms cause flow of air volume between bubble sizes:

- $S_d(a)$ – dissolution of air into the water.
- $S_f(a)$ – fragmentation of bubbles.
- $S_c(a)$ – coalescence of bubbles.

And two mechanisms cause flow of air across the free surface:

- $I(a)$ – injection of bubble through entrainment at the free surface.
- $D(a)$ – loss of bubbles through degassing at the free surface.

In this work, we focus on fragmentation.

It is common to split $S_f(a)$ into two terms, a negative term describing bubbles of size a fragmenting into smaller bubbles and a positive term describing bubbles of size a being created as the daughter of the fragmentation of parents of size $a' > a$:

$$S_f(a) = -\Omega(a)N(a) + \int_a^\infty m(a')f(a;a')\Omega(a')N(a')\,\mathrm{d}a'\,, \quad (3)$$

where $\Omega(a')$ is the fragmentation rate of a bubble of size a', $m(a')$ is the number of daughter bubbles created by the fragmentation of a bubble of size a', and $f(a;a')$ is the radius-based probability density function (p.d.f.) describing the distribution of daughter-bubble radii a created by the breakup of a bubble of size a' (Liao & Lucas, 2009; Martínez-Bazán, *et al.*, 2010). Each of these three functions gives rise to a constant in equation (1), as described below.

Fragmentation Rate

There are multiple mechanisms which can cause fragmentation; however, for typical air-water flows, the dominant (and typically assumed to be the only) cause of fragmentation is bubbles interacting with local turbulent fluctuations (Liao & Lucas, 2009). Assuming the Kolmogorov inertial sub range provides the relationship between the velocity of the turbulent fluctuations at the length-scale of a parent bubble of radius a and the turbulent dissipation rate ε. The parent-bubble Weber number,

$$We_P(a) = \frac{2\varepsilon^{2/3}(2a)^{5/3}}{\sigma/\rho_w}\,, \quad (4)$$

gives the balance between the turbulent fluctuations and surface tension acting on a bubble. For $We_P < We_c$ fragmentation is largely prevented by surface tension. Experiments give $We_c = 4.7$ (Martínez-Bazán, *et al.*, 1999a; Lewis & Davidson, 1982), and the bubble radius a_H corresponding to We_c is the Hinze scale (Hinze, 1955).

In this work, we focus on fragmentation of large bubbles, $We_P \gg We_c$ ($a \gg a_H$). In this regime, the restoring force of surface tension is negligible and dimensional analysis gives the expected lifetime of a

[1] Effective radius a is defined in terms of a bubbles volume V by $a = (3V/4\pi)^{1/3}$.

bubble as $t_b(a) \propto \varepsilon^{-1/3} a^{2/3}$ (Martínez-Bazán, *et al.*, 1999a; Garrett, *et al.*, 2000). The reciprocal of $t_b(a)$ gives the fragmentation rate

$$\Omega(a) = C_\Omega \, \varepsilon^{1/3} \, a^{-2/3} \, , \tag{5}$$

where C_Ω is a scaling constant. Although different models exist for the fragmentation rate, many converge to equation (5) for $We_P \gg We_c$ (Martínez-Bazán, *et al.*, 1999a). Previous experiments give $C_\Omega = 0.42$ (Martínez-Bazán, *et al.*, 1999a; Rodríguez-Rodríguez, *et al.*, 2006).

Number of Daughter Bubbles

The majority of fragmentation models treat $m(a')$, the number of daughter bubbles created by the fragmentation of a parent of radius a', as a deterministic function, specifically, they assume that all fragmentation events are binary, i.e., $m = 2$ (Liao & Lucas, 2009). Theoretically, no events can be perfectly instantaneous, so any non-binary fragmentation events could also be interpreted as a series of rapid binary events. This is an undesirable interpretation because the series of binary fragmentation events would not be statistically independent and would lead to a fragmentation model that could not be easily expressed in the form of equation (3) (Solsvik, *et al.*, 2016).

Recent experimental work on fragmentation has allowed a range of m and examined the resulting statistical distribution (Vejražka, *et al.*, 2018; Qi, *et al.*, 2020). These measurements are sensitive to the snapshot interval Δt_s used by the bubble-tracking method. Too short a Δt_s will lead to statistically interdependent fragmentation events. Too long a Δt_s will inflate the typical value of m. An overly large snapshot interval will view multiple statistically independent fragmentation events as a single event with a significantly larger m number of daughter bubbles (Solsvik, *et al.*, 2016; Vejražka, *et al.*, 2018).

As concluded by Solsvik, *et al.* (2016), the dependence of the distribution of m on the chosen Δt_s for measurement suggests a more robust description of fragmentation is needed. In this paper, we will use a similar description as (Gaylo, *et al.*, 2021), modified to include a statistical distribution of m in equation (8). While the statistics for m depend on the chosen Δt_s, whether the net effect of the fragmentation statistics on τ_c, i.e., $(\ln m)^{-1}(C_f/C_\Omega)$, depends on Δt_s is an open question for future work.

Daughter Bubble-Size Distribution

Equation (3) is written in terms of radius, including the radius-based p.d.f. $f(a;a')$ for the daughter bubble-size distribution. The sum of the volume of the daughter bubbles must equal the parent bubble, so it is more convenient to use a volume-based p.d.f. $f_V^*(V^*, a)$ to describe the daughter bubble-size distribution (Martínez-Bazán, *et al.*, 2010). This is related to the radius-based p.d.f by

$$a f(a';a) = 3V^{*2/3} f_V^*(V^*, a) \, , \tag{6}$$

where $V^* = (a'/a)^3$.

A challenge in fragmentation modeling is that there are many divergent models available for $f_V^*(V^*, a)$ based on a variety of empirical, statistical, and phenomenological arguments (Liao & Lucas, 2009). Although inaccurate, a simple deterministic model is identical fragmentation (Valentas, *et al.*, 1966), where all daughter bubbles are of the same size. The corresponding p.d.f. is a delta function: $f_V^*(V^*) = \delta(V^* - 1/m)$. The deterministic nature allows analysis of the evolution of the bubble-size distribution (Gaylo, *et al.*, 2021).

We have previously shown that the effect of more realistic p.d.f.s compared to the effect of identical fragmentation can be captured by the distribution constant

$$C_f = \frac{\ln(m)/m}{\int_0^1 \int_0^1 uw f_V^*(uw) \, \mathrm{d}w \, \mathrm{d}u} \, , \tag{7}$$

which quantifies how different p.d.f.s changes the time scale to reach equilibrium (equation (1)). For a fixed C_f, different p.d.f.s have little effect on the observed bubble-size distribution $N(a)$, especially at equilibrium (Gaylo, *et al.*, 2021). Table 1 shows values of C_f for selected daughter distributions from literature, illustrating a wide range in predicted values.

Table 1: Gaylo, *et al.* (2021) calculations of daughter bubble-size distribution constant, C_f, for selected daughter distributions at $We_P \sim \infty$ limit.

Daughter bubble-size distribution	m	C_f
Valentas, *et al.* (1966)	any	1
Martínez-Bazán, *et al.* (1999b)	2	1.314
Tsouris & Tavlarides (1994)	2	2.255
Martínez-Bazán, *et al.* (2010)	2	1.712
Diemer & Olson (2002)	3	1.253
Diemer & Olson (2002)	4	1.185

MODELING A DISTRIBUTION OF NUMBER OF DAUGHTER BUBBLES

We now seek to extend the aforementioned fragmentation modeling to include a stochastic description for the number of daughter bubbles m. We modify equation (3) to include $\Pr\{m; a'\}$, the probability a bubble of effective radius a'

will produce m daughter bubbles:

$$S_f(a) = -\Omega(a)N(a) + \sum_{m=2}^{\infty}\int_a^{\infty} m\,\Pr\{m;a'\}f(a;a',m)\Omega(a')N(a')\,\mathrm{d}a' , \tag{8}$$

As in Gaylo, *et al.* (2021), we assume that non-dimensionalized fragmentation is independent of the size of the parent bubble $a' >> a_H$, thus $\Pr\{m;a'\} = \Pr\{m\}$ and the volume-based daughter bubble-size p.d.f. is $f_V^*(V^*;a',m) = f_V^*(V^*;m)$.

Using equation (8) and otherwise following the derivation in Gaylo, *et al.* (2021), the resulting critical time τ_c is now

$$\tau_c = \frac{(9/2)(1/C_\Omega)\varepsilon^{-1/3}{a_{max}}^{2/3}}{\sum_{m=2}^{\infty}\Pr\{m\}m\int_0^1\int_0^1 uw f_V^*(uw;m)\,\mathrm{d}w\,\mathrm{d}u} . \tag{9}$$

We define the effective number of daughter bubbles $\tilde{m}$ based on the expected value $\mathbb{E}\{\ln(m)\} \equiv \ln\tilde{m}$, which gives

$$\tilde{m} = \prod_{m=2}^{\infty} m^{\Pr\{m\}} , \tag{10}$$

and we define the effective distribution constant $\tilde{C}_f$,

$$\frac{1}{\tilde{C}_f} = \sum_{m=2}^{\infty}\Pr\{m\}\frac{m\int_0^1\int_0^1 uw f_V^*(uw;m)\,\mathrm{d}w\,\mathrm{d}u}{\ln(\tilde{m})} . \tag{11}$$

Recalling equation (7), $\tilde{C}_f$ can be expressed as a weighted harmonic average of $C_f(m)$:

$$\frac{1}{\tilde{C}_f} = \sum_{m=2}^{\infty}\Pr\{m\}\frac{\ln m}{\ln\tilde{m}}\frac{1}{C_f(m)} . \tag{12}$$

Using $\tilde{m}$ and $\tilde{C}_f$, we can write equation (9) in the form of equation (1):

$$\tau_c = (9/2)(\ln\tilde{m})^{-1}(\tilde{C}_f/C_\Omega)\;\varepsilon^{-1/3}\,{a_{max}}^{2/3} . \tag{13}$$

For conciseness, we group the three fragmentation constants into a new constant,

$$C_\tau = (9/2)(\ln\tilde{m})^{-1}(\tilde{C}_f/C_\Omega) , \tag{14}$$

to write a compact version of equation (13),

$$\tau_c = C_\tau\;\varepsilon^{-1/3}{a_{max}}^{2/3} . \tag{15}$$

SIMULATION METHODOLOGY

We perform direct numerical simulations of the two-phase, incompressible, three-dimensional Navier-Stokes equations on a uniform Cartesian grid using the conservative Volume of Fluid method (cVOF), while using Eulerian Label Advection (ELA) to track the volume of individual bubbles (Weymouth & Yue, 2010; Gaylo, *et al.*, 2022). This provides a volume-conservative description of the evolution of all bubbles in the simulation in terms of volume transfer between bubbles.

Two-Phase Fluid Solver, cVOF

The velocity field $\mathbf{u}(\mathbf{x},t)$ for an incompressible flow follows the continuity equation $\nabla\cdot\mathbf{u} = 0$ and momentum conservation

$$\frac{\mathrm{D}\mathbf{u}}{\mathrm{D}t} = -\frac{1}{\rho(\mathbf{x})}\nabla p + \frac{1}{Re_T}\frac{1}{\rho(\mathbf{x})}\nabla\cdot(2\mu(\mathbf{x})\mathbf{E}) + \frac{1}{We_T}\kappa\delta_s\mathbf{n} , \tag{16}$$

where p is the pressure field and $\mathbf{E}$ is the rate-of-strain tensor $1/2(\nabla\mathbf{u} + \nabla\mathbf{u}^T)$. When using a finite We_T, surface tension is calculated using a continuous surface force method (Brackbill, *et al.*, 1992) along with a height-function method to calculate the curvature κ (Cummins, *et al.*, 2005; Popinet, 2009).

For immiscible fluids, a Volume of Fluid method is defined based on the fluid color function,

$$c(\mathbf{x},t) = \begin{cases} 1 & \text{if} \quad \mathbf{x}\in\text{'dark' fluid} \\ 0 & \text{if} \quad \mathbf{x}\in\text{'light' fluid} \end{cases} . \tag{17}$$

For these simulations, let air be the 'dark' fluid and water the 'light' fluid. The average of $c(\mathbf{x})$ within the volume Δx^3 of each computational cell gives the volume fraction $f(\mathbf{x})$, from which density and viscosity are calculated

$$\rho(\mathbf{x}) = f(\mathbf{x})\rho_a + [1-f(\mathbf{x})]\rho_w , \tag{18a}$$

$$\mu(\mathbf{x}) = f(\mathbf{x})\mu_a + [1-f(\mathbf{x})]\mu_w . \tag{18b}$$

For air-water, we use $\rho_a/\rho_w = 0.001$ and $\mu_a/\mu_w = 0.01$.

cVOF provides the discrete evolution of $f(\mathbf{x})$ over a time step Δt through an operator-split advection method

$$\Delta f = \frac{\Delta t}{\Delta x^3}\left(\Delta_d F_d + \tilde{c}\frac{\partial u_d}{\partial x_d}\Delta x^3\right) \quad \text{for} \quad d\in 1\ldots 3, \tag{19}$$

where the difference in flux between the two faces in a direction $\Delta_d F_d = F_{d+1/2} - F_{d-1/2}$ is calculated using a second-order interface reconstruction done each operator-split step, and the dilation term is calculated using $\tilde{c}$, the cell-centered approximation of $c(\mathbf{x})$ based on the initial $f(\mathbf{x})$. Choosing a fluid-solver time step Δt which follows the Courant restriction

$$\Delta t\sum_{d=1}^{3}\left|\frac{u_d}{\Delta x}\right| \le \frac{1}{2} \tag{20}$$

guarantees that cVOF conserves the volume of both fluids to machine precision (Weymouth & Yue, 2010).

To develop and maintain IHT, a linear forcing term,

$$\mathbf{f} = A\mathbf{u}\left(1 - f(\mathbf{x})\right) \,, \tag{21}$$

is added to equation (16), where A is chosen to achieve a desired turbulent dissipation rate, ε (Lundgren, 2003; Rosales & Meneveau, 2005). Following Rivière, *et al.* (2021), the forcing only acts on regions of water.

We discretize the governing equations using a staggered-grid finite-volume method with second-order central differences for the convective terms and an explicit second-order predictor-corrector method estimates the time integral in equation (16). The pressure is determined from the continuity equation using the projection method. This pressure Poisson equation is solved using the *hypre* library (Falgout, *et al.*, 2006). Yu, *et al.* (2019) provide the numerical verification of this method for simulating fragmenting bubbly-flow including surface tension.

Tracking Bubble Evolution, ELA

Tracking bubble evolution has two parts: first we identify contiguous connected regions of air, i.e., bubbles, and assign them each a unique label j, and second, we track how the bubble volume flows through time. Identifying contiguous connected regions of air is, more generally, the process of connected-component labeling (CCL) (He, *et al.*, 2017). For these simulations we use the informed component labeling method (ICL) (Hendrickson, *et al.*, 2020) which, in addition to requiring adjacent computational cells to both have non-zero volume fraction to be considered connected, requires their interface normals not to be opposed. This method has the advantage of being conservative in that all air volume is identified as part of a bubble. However, this means it includes non-physical wisps, numerical artifacts of finite-precision interface reconstruction (Chan, *et al.*, 2021). To avoid the computational cost of tracking these non-physical structures, we ignore bubbles identified by ICL with volumes $v_j < \Delta x^3$.

Tracking where the bubble volume flows through time is provided by ELA (Gaylo, *et al.*, 2022). Based on the regions of air identified as bubbles using ICL at a time $t = t^n$, similar to equation (17), ELA defines a vector color function $\mathbf{c}^n(\mathbf{x})$ with components corresponding to each label i assigned by ICL and given at t^n by

$$c_j^n(\mathbf{x}, t^n) = \begin{cases} 1 & \text{if} \quad \mathbf{x} \in \text{bubble } j \\ 0 & \text{else} \end{cases} \,. \tag{22}$$

The vector equivalent of the void fraction $f(\mathbf{x})$ is the source vector $\mathbf{s}^n(\mathbf{x})$, the average of $\mathbf{c}^n(\mathbf{x})$ within a computational cell. Analogous to cVOF, ELA provides the evolution of $\mathbf{s}^n(\mathbf{x})$ through an operator-split advection method

$$\Delta\mathbf{s}^n = \frac{\Delta t}{\Delta x^3}\left(\Delta_d \mathbf{F}_d + \tilde{\mathbf{c}}\frac{\partial u_d}{\partial x_d}\Delta x^3\right) \quad \text{for} \quad d \in 1\ldots 3 \,. \tag{23}$$

The first (vector flux) term uses $\mathbf{F}_{d+1/2}$ calculated by splitting the analogous cVOF flux term using the $\mathbf{s}^n$ from the previous operator-split step,

$$\mathbf{F}_{d+1/2} = F_{d+1/2} \cdot \begin{cases} \frac{\mathbf{s}^n_{d+1}}{\|\mathbf{s}^n_{d+1}\|} & \text{if} \quad F_{d+1/2} > 0 \\ \frac{\mathbf{s}^n_{d}}{\|\mathbf{s}^n_{d}\|} & \text{if} \quad F_{d+1/2} < 0 \end{cases} \,. \tag{24}$$

The second (vector dilation) term in equation (23) uses $\tilde{\mathbf{c}}$ calculated by splitting the analogous cVOF term based on the initial $\mathbf{s}^n$,

$$\tilde{\mathbf{c}} = \tilde{c}\,\frac{\mathbf{s}^n}{\|\mathbf{s}^n\|} \,. \tag{25}$$

Applying same Courant restriction in equation (20) also guarantees that ELA conserves the volume of the air tracked by $\mathbf{s}^n$ to machine precision (Gaylo, *et al.*, 2022).

ELA evolves $\mathbf{s}^n$ over a prescribed snapshot time-interval $\Delta t_s \gg \Delta t$. At time $t^{n+1} = t^n + \Delta t_s$, ICL and equation (22) again provide a new source vector $\mathbf{s}^{n+1}(\mathbf{x})$ based on the bubbles present at t^{n+1}, given labels i. We write the flow of volume from a bubble j at time t^n to a bubble i at time t^{n+1} as

$$q_{ij}^n = \int_{\forall} s_i^{n+1}(\mathbf{x}) s_j^n(\mathbf{x})\,\mathrm{d}V \,, \tag{26}$$

where $\forall$ is the whole domain (Gaylo, *et al.*, 2022). This provides a complete description of the flow of air from bubbles at time t^n to bubbles at time t^{n+1} and provides the description of the evolution of the bubble population over the prescribed snapshot interval Δt_s. We save a tracking-matrix representation $\mathbf{Q}^n = \{q_{ij}^n\}$ at every Δt_s in compressed sparse row (CSR) format for post-processing.

Extracting Fragmentation Statistics

Each tracking-matrix $\mathbf{Q}^n$ provides the detailed information for all the fragmentation events between t^n and t^{n+1} through multiple non-zero entries in a single column. The value of each entry represents the volume from one parent bubble at t^n (with label j corresponding to index of the column of $\mathbf{Q}^n$) existing in a daughter bubble at t^{n+1} (with label i corresponding to index of the non-zero row in the column j). In detail, the size of each daughter bubble v_i from the breakup of a parent bubble with label j and volume v_j is given by the non-zero q_{ij}^n. From each fragmentation event, we extract the set of non-dimensionalized daughter bubbles

$$V^* = \{q_{ij}^n / v_j : q_{ij}^n \neq 0\} \,, \tag{27}$$

and the length of the set gives us the number of daughter bubbles m from the fragmentation event.

Reasonable limitations of numerical grids combined with no pre-defined limit for the smallest possible daughter bubble results in an inability to fully resolve all fragmentation events. Thus, following Yu, *et al.* (2019), we define a minimum resolved-bubble volume $v_{\text{res}} = 4/3\pi(1.5\Delta x)^3$ for calculating these statistics. Only fragmentation of parents j where *all* daughter bubbles have volume $q_{ij}^n > v_{\text{res}}$ are considered resolved fragmentation events.

SIMULATION SETUP

Using cVOF and ELA, we perform an ensemble of simulations of bubbles fragmenting in IHT at a turbulent Reynolds number, $Re_T = (u_{\text{rms}}^4)/(\varepsilon\nu_w)$, of 200 and different turbulent Weber numbers, $We_T = (\rho_w u_{\text{rms}}^5)/(\varepsilon\sigma)$ (to provide a variable We_P for our analysis.) We non-dimensionalize these simulations based on the characteristic dissipation rate $\varepsilon \equiv 1$ and root-mean-squared velocity magnitude $u_{\text{rms}} \equiv 1$ to define the forcing magnitude A in equation (21). The domain is a triply-periodic cube with dimension $L = 5.28$ and we use two different grid resolutions (coarse (c) $\Delta x_c/L = 1/128$ and fine (f) $\Delta x_f/L = 1/256$) to establish convergence. The fine grid effectively resolves the Kolmogorov length scale $\eta \sim \varepsilon^{-1/4}\nu_w^{3/4}$. Both grids sufficiently resolve the interface curvature based on the cell Weber number $We_\Delta = (\rho_w u_{\text{rms}}^2 \Delta x)/(4\pi\sigma)$ (Popinet, 2018). A summary of the simulation parameters and the multiple grid resolutions used in this paper is in table 2.

We initialize the cVOF simulation following Yu, *et al.* (2019) by first developing a single-phase IHT field from white noise. The flow evolves in time with the linear IHT forcing term (21) until a quasi-steady state has been reached with the desired ε. To this flow field, we add a randomly distributed non-overlapping population of spherical bubbles with radii randomly distributed between $a_{min} = 3\Delta x_f$ and $a_{max} = 15\Delta x_f$ following the commonly observed $N(a) \propto a^{-10/3}$ power law (Garrett, *et al.*, 2000; Deane & Stokes, 2002). The resulting total void fraction in the domain is 1%. The simulations are run until $t = 4\tau$, where $\tau = t_b(a_0)$ is the characteristic fragmentation time of the measured parent bubbles (radius a_0) based on equation (5) assuming the experimentally provided $C_\Omega = 0.42$ (Martínez-Bazán, *et al.*, 1999a; Rodríguez-Rodríguez, *et al.*, 2006). To ensure we consider the fragmentation of naturally fragmenting non-spherical bubbles, we only consider data in the period $1 < t/\tau < 4$. The ensemble simulations represent 4 different realizations of the bubble population using the same developed IHT velocity field as the initial condition.

For our analysis, we consider fragmentation events where the parent bubbles have a radius $a_0 < a < a_1$, where $a_0 = 6\Delta x_f = 0.124$ (giving $\tau = 0.59$) and $a_1 = 1.2a_0$. We choose a fixed a_0 to provide a consistent numerical resolution at all We_P on each grid and facilitate convergence studies across grids.

Figure 1 shows the resulting bubble-size distribution for the fine-grid simulations compared to the the commonly observed $N(a) \propto a^{-10/3}$ power law. The fragmentation of bubbles with radius $a > a_0$ maintains the population of bubbles of radius $\sim a_0$. Thus, the parent bubbles we measure are created by the same fragmentation cascade found during entrainment (Garrett, *et al.*, 2000), which is the dominant creation mechanism for bubbles $a \ll a_{max}$ during weak entrainment (Gaylo, *et al.*, 2021). This establishes that the period $1 < t/\tau < 4$ provides realistic fragmentation events for our analysis.

An important factor in defining a single fragmentation event versus a chain of fragmentation events is the snapshot interval Δt_s used by the bubble-tracking method (Solsvik, *et al.*, 2016; Vejražka, *et al.*, 2018). Chan, *et al.* (2021) recommend $\Delta t_s/\tau = 1/10$ for numerical simulations. Understanding that the choice of Δt_s has a strong influence on fragmentation statistics, we follow Chan, *et al.* (2021) which leads to a good agreement between our observed distribution of m and experiments by Qi, *et al.* (2020). We note that this choice leads to a poor agreement with experiments by Vejražka, *et al.* (2018), who used a fixed Δt_s independent of τ, leading to a different definition of what constitutes a single fragmentation event.

All simulations were performed with the grid distributed over 64 cores on 2 nodes of an HPE (Hewlett Packard Enterprise Co.) SGI 8600 system located the U.S. Navy DoD Supercomputing Resource Center (Navy DSRC). In total 40,000 CPU hours were used for the simulations of this work.

RESULTS

Fragmentation Rate

We start by evaluating the observed fragmentation rate to provide an estimate of C_Ω. For a bubble of radius $r = a$ that exists at the start of a snapshot interval, if there is a constant fragmentation rate $\Omega(a) = 1/t_b(a)$, then the probability the bubble will fragment during a the snapshot interval is given by a Poisson arrival rate process,

$$\Pr\{\text{frag.} \mid r = a\} = 1 - \exp\left[-\Delta t_s/t_b(a)\right] . \qquad (28)$$

As we choose $\Delta t_s/\tau$ by assuming $C_\Omega = 0.42$, equation (5) allows us to write,

$$\Pr\{\text{frag.} \mid r = a\} = 1 - \exp\left[-\frac{\Delta t_s}{\tau}\frac{C_\Omega}{0.42}\left(\frac{a}{a_0}\right)^{-2/3}\right], \qquad (29)$$

where C_Ω here is the value of C_Ω implied by $\Pr\{\text{frag.} \mid r = a\}$.

Table 2: Summary of simulations performed.

Initial IHT Field				Fragmentation Simulation						
Grid	Re_T	$\Delta x/L$	$\Delta x/\eta$	We_T	We_Δ	We_P	$\Delta t_s/\tau$	# of Simulations	# of Frag. Events	
									Total	Resolved
c	200	1/128	2.2	∞	-	∞	1/10	4	1071	103
				400	1.31	78 – 106	1/10	4	1075	97
				200	0.66	39 – 53	1/10	4	1151	130
f	200	1/256	1.1	∞	-	∞	1/10	4	989	81
				400	0.66	78 – 106	1/10	4	1116	113
				200	0.33	39 – 53	1/10	4	1134	128

Table 3: Measured fragmentation rate constant, $(C_\Omega)_{\text{sim}}$, based on resolved fragmentation events.

We_P	Grid	C_Ω	95% C.I.
∞	c	0.34	0.28 – 0.41
	f	0.29	0.22 – 0.35
78 – 106	c	0.31	0.25 – 0.38
	f	0.36	0.29 – 0.43
39 – 53	c	0.41	0.34 – 0.48
	f	0.39	0.32 – 0.46

As the bubbles in the range of interest $a_0 < a < a_1$ follow a $-10/3$ power law (see figure 1) the p.d.f. is,

$$f(a) = \frac{\mathrm{d}}{\mathrm{d}a}\Pr\{r = a \mid a_0 < r < a_1\} = \frac{1}{a_0}\left(\frac{a}{a_0}\right)^{-10/3}\frac{7/3}{1-(a_1/a_0)^{-7/3}}\,. \quad (30)$$

The probability of fragmentation for any parent bubble of radius $a_0 < a < a_1$ is

$$\Pr\{\text{frag.}\} = \int_{a_0}^{a_1} f(a)\Pr\{\text{frag.} \mid r = a\}\,\mathrm{d}a\,, \quad (31)$$

This gives us an implicit equation involving incomplete gamma functions which we solve (numerically) to give C_Ω based on Pr{frag.} (and the associated confidence interval) provided by comparing the number of resolved fragmentation events recorded by ELA to the number of parent bubbles present each snapshot interval.

Table 3 shows the measured fragmentation rate for all We_P on different grids with the 95% confidence interval. We observe $C_\Omega \approx 0.3 - 0.4$, and the confidence interval suggests these results could still be consistent with $C_\Omega = 0.42$ from experiments (Martínez-Bazán, *et al.*, 1999a; Rodríguez-Rodríguez, *et al.*, 2006).

Table 4: Measured average daughter bubble count $\mathbb{E}\{m\}$ and effective daughter bubble count $\tilde{m}$ given by equation (10) for resolved fragmentation events. The 95% confidence interval is included for $\mathbb{E}\{m\}$.

We_P	Grid	$\mathbb{E}\{m\}$	$\tilde{m}$	$\ln(\tilde{m})$
∞	c	2.38 ± 0.07	2.31	0.84
	f	2.43 ± 0.08	2.34	0.85
78 – 106	c	2.31 ± 0.06	2.25	0.81
	f	2.41 ± 0.07	2.32	0.84
39 – 53	c	2.25 ± 0.05	2.20	0.79
	f	2.29 ± 0.06	2.22	0.80
Qi, *et al.* (2020)		2.36	2.27	0.82

Number of Daughter Bubbles

We now evaluate the number of daughter bubbles m created by resolved fragmentation events. The number of daughter bubbles is available directly from ELA for each fragmentation event as the number of entries in V^* from equation (27). We confirm numerical convergence of the distribution of m at each We_T by comparing the course and fine grid results (see figure 2). The 95% confidence interval quantifies the statistical convergence.

Figure 3 compares the measured distribution of m across different Weber numbers (for the fine grid simulations). Table 4 reports the measured expected value of m as well as the effective value $\tilde{m}$ given by equation (10). The consistency between the $We_P \sim \infty$ and the larger finite We_P simulation suggest that for $We_P > O(100)$ $\ln\tilde{m} \approx 0.85$. When we include the smaller finite We_P simulations as well as the experimental results of Qi, *et al.* (2020) who looked at $1.1 < We_P < 5.2$, we find the range $\ln(\tilde{m}) \approx 0.80 - 0.85$. We note that the relatively small influence of We_P on the distribution of m observed in figure 3 conflicts with the empirical fit proposed by Vejražka, *et al.* (2018), which uses a Δt_s independent of the characteristic parent-bubble fragmentation time.

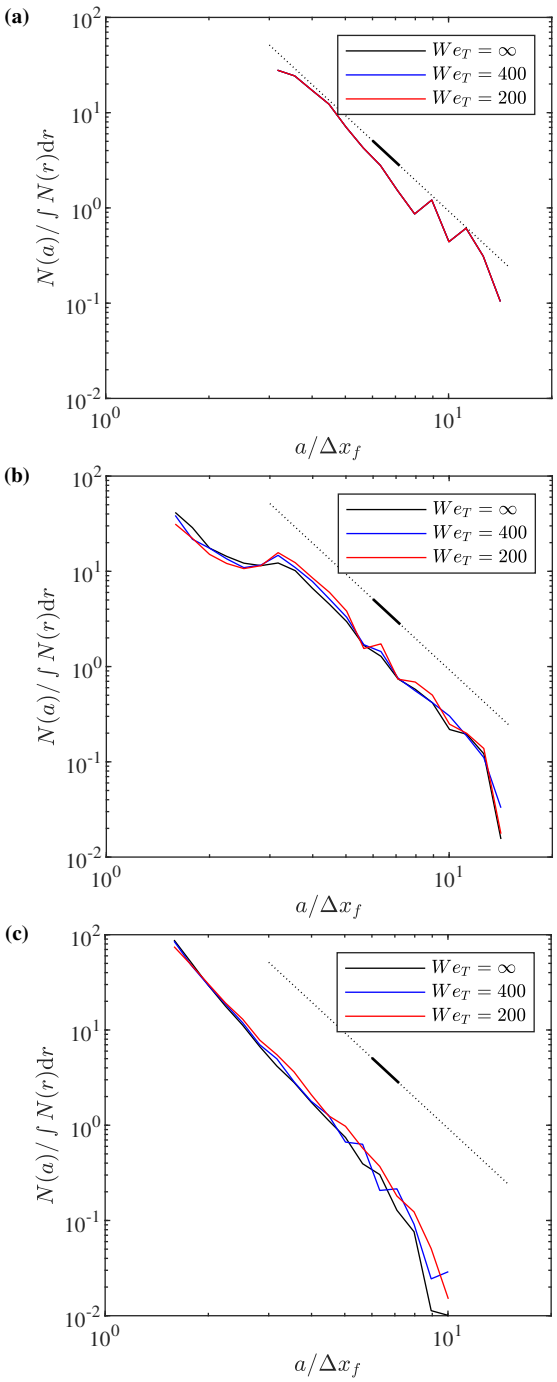

Figure 1: Normalized bubble-size distribution $N(a)$ at (a) $t/\tau = 0$, (b) $t/\tau = 1$, and (c) $t/\tau = 4$ from the ensemble of fine-grid simulations. In (a) all lines overlap. The dotted line shows an $a^{-10/3}$ power law over $a_{min} < a < a_{max}$, and the solid portion denotes $a_0 < a < a_1$. Note that only resolved bubbles ($a > 1.5\Delta x_f$) are included.

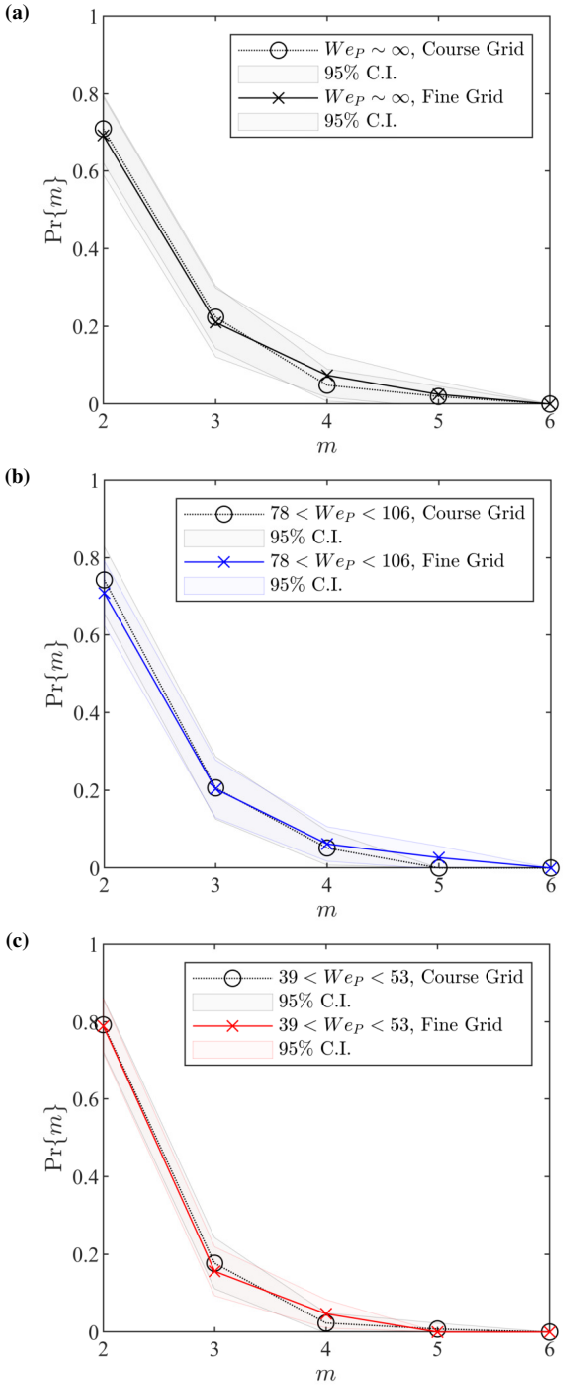

Figure 2: Comparison of the probability distribution of the number of daughter bubbles m observed in resolved fragmentation events between the course and fine gird for (a) $We_T = \infty$, (b) $We_T = 400$ and (c) (b) $We_T = 200$.

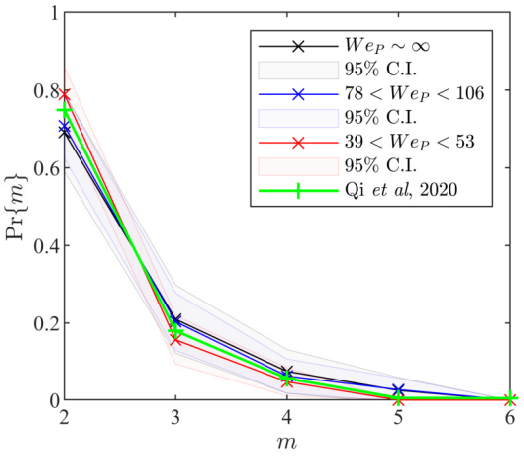

Figure 3: Probability distribution of the number of daughter bubbles m observed in resolved fragmentation events from the fine-grid simulations compared to experimental observations by Qi, *et al.* (2020).

Table 5: Effective daughter distribution constant $\tilde{C}_f$ given by equation (12) for resolved fragmentation events.

We_P	Grid	$\tilde{C}_f$
∞	f	2.35
78 – 106	f	2.22
39 – 53	f	2.14

Daughter Bubble-Size Distribution

We now evaluate the daughter bubble-size distributions of resolved fragmentation events to measure the value of $\tilde{C}_f$ using equation (12). From ELA, for V^* with m entries, each entry represents a sample from the corresponding daughter-size distribution $f_V^*(V^*;m)$, shown in figure 4.

In figure 5 we show the constants $C_f(m)$ for each m calculated by equation (7), the property of the daughter bubble-size distributions relevant to τ_c. In comparison with the $C_f(m)$ calculated using existing daughter distributions models in table 1 (Gaylo, *et al.*, 2021) for $m = 2$, we note a consistently larger value except for that by Tsouris & Tavlarides (1994) who gives a ∪-shaped distribution similar to that in figure 4. As most fragmentation models assume $m = 2$ (Liao & Lucas, 2009), there are a limited number of previous models to compare to our $C_f(m > 2)$ results.

Using each $C_f(m)$ as well as the measured distribution of m discussed in the previous section, equation (12) allows us to calculate the effective daughter bubble-size distribution constant $\tilde{C}_f$. The results, shown in table 5, show that $\tilde{C}_f$ increases slightly with We_P, but all results for the We_P considered fall within $\tilde{C}_f \approx$

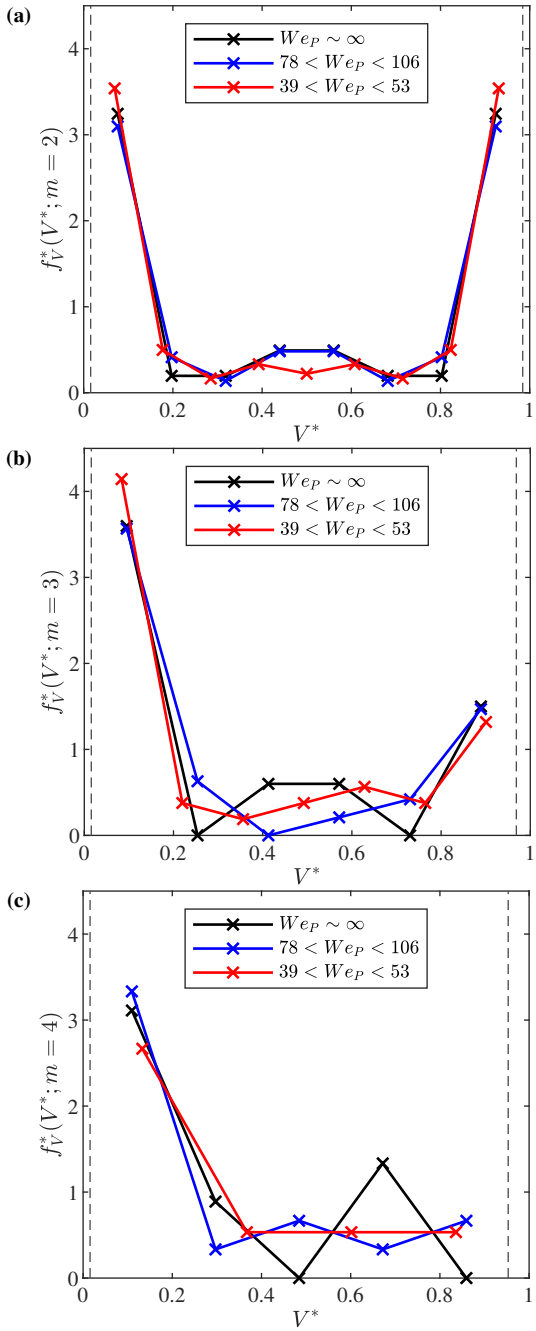

Figure 4: Non-dimensionalized volume-based daughter bubble-size p.d.f. $f_V^*(V^*;m)$ for (a) $m = 2$, (b) $m = 3$, and (c) $m = 4$ based on resolved fragmentation events from the fine-grid simulations. The dashed lines indicated the resolution limits. Number of bins chosen using Sturges' rule.

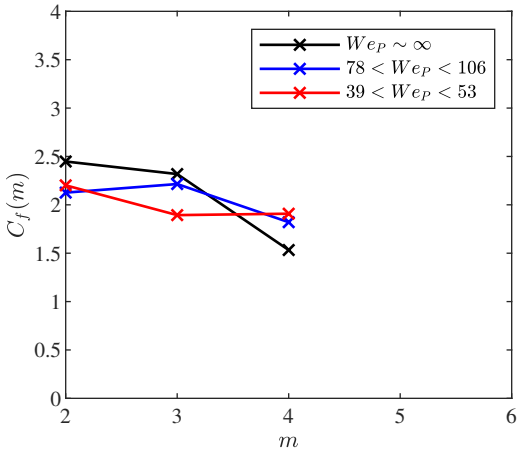

Figure 5: The daughter distribution constant $C_f(m)$ given by equation (7) for each number of daughter bubbles m observed in resolved fragmentation events from the fine-grid simulations.

Table 6: Summary of measured fragmentation statistics for $We_P \sim \infty$ on the fine grid.

Fragmentation property	Measure	Value
Fragmentation rate	C_Ω	0.29
Number of daughter bubbles	$\ln \tilde{m}$	0.85
Daughter bubble-size distribution	$\tilde{C}_f$	2.35

2.1 – 2.4. This suggests that, as with the other properties of fragmentation, there is relatively little dependence of the relevant characteristics of the daughter bubble-size distribution on $We_P > 39$.

DISCUSSION

Our analysis of each of the three fragmentation measures enables us to investigate the net effect of fragmentation on τ_c through C_τ. Our interest is modeling $We_P \gg We_c$, and we find little variation in the fragmentation measures over the range of $We_P > 39$ ($a/a_H > 3.6$). Thus, we focus on the limiting case of $We_P \sim \infty$. We use equation (14) and the $We_P \sim \infty$ results, summarized in table 6, to calculate $C_\tau \approx 43$.

We finish with brief illustration of the magnitude and potential application of τ_c using this C_τ. From simulations of the wake around *R/V Athena*, a 47 m converted Asheville-class patrol gunboat, traveling at $U = 10.5$ knots (5.4 m/s), Castro, *et al.* (2016) reported $\varepsilon = 3.3\,\mathrm{W\,kg^{-1}}$ in the wake of the transom stern and suggested $a_{max} \sim 1$ cm. Using equation (15), this gives $\tau_c \approx 1.3$ s. This shows that the transient state of the bubble-size distribution as it converges to equilibrium is rapid, but observable. For example, in the frame of reference of this vessel traveling at 10.5 knots, this suggests a characteristic length-scale on the order of $L \sim U\tau_c \approx 7$ m within which the transient behavior of the bubble-size distribution (in the absence of other mechanisms like degassing) is observable. Beyond this distance from the start of the entrainment region (e.g., bow and transom), the resulting bubble-cloud follows the well-described equilibrium bubble-size distribution.

CONCLUSION

This paper studies fragmentation of air-water bubbles in turbulence to quantify the scaling constant for the timescale τ_c (Gaylo, *et al.*, 2021), which describes how long it takes for the distribution of large bubbles ($We_P \gg We_c$) to reach an equilibrium in bubbly-flows dominated by turbulent free-surface entrainment and fragmentation, such as the near-wake of surface vessels and near-surface submarines. We show that $\tau_c = C_\tau\ \varepsilon^{-1/3} {a_{max}}^{2/3}$, where a_{max}, the largest bubble injected by entrainment, captures the effect of entertainment, ε, the turbulent dissipation rate, captures the effect of turbulence, and the scaling constant C_τ captures three non-dimensional measures of the fragmentation process (see equation (14)).

Existing models of fragmentation do not agree on the relevant measures of fragmentation, and few are able to describe fragmentation including a statistical distribution for the number of daughter bubbles. We perform direct numerical simulations of bubbles fragmenting at a range of $We_P \gg We_c$ ($a \gg a_H$) and, using Eulerian Label Advection (Gaylo, *et al.*, 2022), are able to measure the complete description of all resolved fragmentation events, including those with more than two daughter bubbles. This allows us to directly calculate the relevant measures of fragmentation (C_Ω, $\tilde{m}$, and $\tilde{C}_f$) that leads finally to C_τ.

Using our results, we calculate the scaling constant for τ_c to be $C_\tau \approx 43$, which we show is relatively independent of $We_P > 39$. This result combined with knowledge of the upper-bound of bubbles created by entrainment and the strength of turbulence in a ship wake provides insight into a timescale, and by extension a length-scale relevant to predicting the resulting bubble-size distribution.

One critical area of uncertainty left remaining in this research effort is the dependence of the fragmentation measurements on the chosen snapshot interval Δt_s (Solsvik, *et al.*, 2016; Vejražka, *et al.*, 2018). The choice of Δt_s influences individual fragmentation measurements, but it is unknown what the net effect is on the measurement of C_τ. Understanding the influence of Δt_s on the underlying fragmentation measurements is a focus of our current research to ensure an accurate estimate of C_τ and thus τ_c for CSH.

ACKNOWLEDGMENTS

This work was funded by the U.S. Office of Naval Research grant N00014-20-1-2059 under the guidance of Dr. W.-M. Lin. This work was supported in part by high-performance computer time and resources from the DoD High Performance Computing Modernization Program.

REFERENCES

Brackbill, J., Kothe, D., and Zemach, C., "A continuum method for modeling surface tension," J. Comput. Phys., Jun. 1992, Vol. 100, No. 2, pp. 335–354.

Castro, A.M., Li, J., and Carrica, P.M., "A mechanistic model of bubble entrainment in turbulent free surface flows," Int. J. Multiphase Flow, 2016, Vol. 86, pp. 35–55.

Chan, W.H.R., Dodd, M.S., Johnson, P.L., and Moin, P., "Identifying and tracking bubbles and drops in simulations: A toolbox for obtaining sizes, lineages, and breakup and coalescence statistics," J. Comput. Phys., 2021, Vol. 432, p. 110156.

Cummins, S.J., Francois, M.M., and Kothe, D.B., "Estimating curvature from volume fractions," Comput. Struct., Feb. 2005, Vol. 83, No. 6-7, pp. 425–434.

Deane, G.B. and Stokes, M.D., "Scale dependence of bubble creation mechanisms in breaking waves," Nature, 2002, Vol. 418, pp. 839–844.

Deike, L., Melville, W.K., and Popinet, S., "Air entrainment and bubble statistics in breaking waves," J. Fluid Mech., 2016, Vol. 801, pp. 91–129.

Diemer, R.B. and Olson, J.H., "A moment methodology for coagulation and breakage problems: Part 3—generalized daughter distribution functions," Chem. Eng. Sci., 2002, Vol. 57, pp. 4187–4198.

Falgout, R., Jones, J., and Yang, U., "The Design and Implementation of *hypre*, a Library of Parallel High Performance Preconditioners," A. Bruaset and A. Tveito, (eds.) Numerical Solution of Partial Differential Equations on Parallel Computers, Vol. 51, Springer-Verlag, 2006, pp. 267–294.

Garrett, C., Li, M., and Farmer, D., "The Connection between Bubble Size Spectra and Energy Dissipation Rates in the Upper Ocean," J. Phys. Oceanogr., 2000, Vol. 30, No. 9, pp. 2163–2171.

Gaylo, D.B., Hendrickson, K., and Yue, D.K., "Effects of power-law entrainment on bubble fragmentation cascades," J. Fluid Mech., Jun. 2021, Vol. 917, No. 9, p. R1.

Gaylo, D.B., Hendrickson, K., and Yue, D.K., "An Eulerian label advection method for conservative volume-based tracking of bubbles/droplets," J. Comput. Phys., Aug. 2022, Vol. 470, p. 111560.

He, L., Ren, X., Gao, Q., Zhao, X., Yao, B., and Chao, Y., "The connected-component labeling problem: A review of state-of-the-art algorithms," Pattern Recognit., 2017, Vol. 70, pp. 25–43.

Hendrickson, K., Weymouth, G.D., and Yue, D.K., "Informed component label algorithm for robust identification of connected components with volume-of-fluid method," Comput. Fluids, 2020, Vol. 197, p. 104373.

Hendrickson, K., Yu, X., and Yue, D.K., "Modelling entrainment volume due to surface-parallel vortex interactions with an air–water interface," J. Fluid Mech., May 2022, Vol. 938, p. A12.

Hesketh, R.P., Etchells, A.W., and Russell, T.W.F., "Experimental observations of bubble breakage in turbulent flow," Ind. Eng. Chem. Res., May 1991, Vol. 30, No. 5, pp. 835–841.

Hinze, J.O., "Fundamentals of the hydrodynamic mechanism of splitting in dispersion processes," AIChE J., 1955, Vol. 1, pp. 289–295.

Lewis, D.A. and Davidson, J.F., "Bubble splitting in shear flow," Trans. Inst. Chem. Eng., 1982, Vol. 60, pp. 283–291.

Liao, Y. and Lucas, D., "A literature review of theoretical models for drop and bubble breakup in turbulent dispersions," Chem. Eng. Sci., 2009, Vol. 64, pp. 3389–3406.

Lundgren, T.S., "Linearly forced isotropic turbulence," Tech. rep., Center for Turbulence Research, Stanford University, 2003.

Martínez-Bazán, C., Montañés, J.L., and Lasheras, J.C., "On the breakup of an air bubble injected into a fully developed turbulent flow. Part 1. Breakup frequency," J. Fluid Mech., 1999a, Vol. 401, pp. 157–182.

Martínez-Bazán, C., Montañés, J.L., and Lasheras, J.C., "On the breakup of an air bubble injected into a fully developed turbulent flow. Part 2. Size PDF of the resulting daughter bubbles," J. Fluid Mech., 1999b, Vol. 401, pp. 183–207.

Martínez-Bazán, C., Rodríguez-Rodríguez, J., Deane, G.B., Montaes, J.L., and Lasheras, J.C., "Considerations on bubble fragmentation models," J. Fluid Mech., 2010, Vol. 661, pp. 159–177.

NDRC, "Acoustic properties of wakes," Physics of Sound in the Sea, Vol. 8, Office of Scientific Research and Development, Washington, D. C., 1946, pp. 441–559.

Popinet, S., "An accurate adaptive solver for surface-tension-driven interfacial flows," J. Comput. Phys., Sep. 2009, Vol. 228, No. 16, pp. 5838–5866.

Popinet, S., "Numerical Models of Surface Tension," Annu. Rev. Fluid Mech., 2018, Vol. 50, No. 1, pp. 49–75.

Qi, Y., Mohammad Masuk, A.U., and Ni, R., "Towards a model of bubble breakup in turbulence through experimental constraints," Int. J. Multiphase Flow, 2020, Vol. 132, p. 103397.

Rivière, A., Mostert, W., Perrard, S., and Deike, L., "Sub-Hinze scale bubble production in turbulent bubble break-up," J. Fluid Mech., Jun. 2021, Vol. 917, p. A40.

Rodríguez-Rodríguez, J., Gordillo, J.M., and Martínez-Bazán, C., "Breakup time and morphology of drops and bubbles in a high-Reynolds-number flow," J. Fluid Mech., 2006, Vol. 548, pp. 69–86.

Rodríguez-Rodríguez, J., Martínez-Bazán, C., and Montañes, J.L., "A novel particle tracking and break-up detection algorithm: application to the turbulent break-up of bubbles," Meas. Sci. Technol., Aug. 2003, Vol. 14, No. 8, pp. 1328–1340.

Rosales, C. and Meneveau, C., "Linear forcing in numerical simulations of isotropic turbulence: Physical space implementations and convergence properties," Phys. Fluids, 2005, Vol. 17, p. 095106.

Solsvik, J., Maaß, S., and Jakobsen, H.A., "Definition of the Single Drop Breakup Event," Ind. Eng. Chem. Res., 2016, Vol. 55, No. 10, pp. 2872–2882.

Trevorrow, M.V., Vagle, S., and Farmer, D.M., "Acoustical measurements of microbubbles within ship wakes," J. Acoust. Soc, Apr. 1994, Vol. 95, No. 4, pp. 1922–1930.

Tsouris, C. and Tavlarides, L.L., "Breakage and coalescence models for drops in turbulent dispersions," AIChE J., 1994, Vol. 40, pp. 395–406.

Valentas, K.J., Bilous, O., and Amundson, N.R., "Analysis of Breakage in Dispersed Phase Systems," Ind. Eng. Chem. Fundamen., 1966, Vol. 5, pp. 271–279.

Vejražka, J., Zedníková, M., and Stanovský, P., "Experiments on breakup of bubbles in a turbulent flow," AIChE J., 2018, Vol. 64, No. 2, pp. 740–757.

Weymouth, G. and Yue, D.K., "Conservative Volume-of-Fluid method for free-surface simulations on Cartesian-grids," J. Comput. Phys., Apr. 2010, Vol. 229, No. 8, pp. 2853–2865.

Yu, X., Hendrickson, K., Campbell, B.K., and Yue, D.K., "Numerical investigation of shear-flow free-surface turbulence and air entrainment at large Froude and Weber numbers," J. Fluid Mech., 2019, Vol. 880, pp. 209–238.

Yu, X., Hendrickson, K., and Yue, D.K., "Scale separation and dependence of entrainment bubble-size distribution in free-surface turbulence," J. Fluid Mech., 2020, Vol. 885, p. R2.

DISCUSSION

Dr. W.H. Ronald Chan, Department of Aerospace Engineering Sciences, University of Colorado Boulder.

The authors have written a very interesting paper that systematically investigates bubble fragmentation in a homogeneous turbulent flow accounting for non-binary breakup events, including comparison with past experiments. Here are several follow-up questions:

1. The model flow that the authors consider does not have active entrainment unlike in Gaylo, *et al.* (2021). How may the time scales for entrainment-driven fragmentation (previous work) and pure fragmentation (current work) be distinguished?

2. Previous work has suggested that large non-spherical parent bubbles tend to generate very small child bubbles in inhomogeneous turbulent flows through non-local breakup events, while equal breakup of smaller parent bubbles (e.g., $We_P \sim 20$) in the inertial subrange is favored. How may the authors incorporate this into their breakup probability distribution, which is currently assumed to be independent of the parent bubble size?

3. The authors have access to a We_P range spanning a factor of about 2.7. How do the authors plan to increase this range to support their hypothesis of We_P independence? How does the range of independent We_P depend on We_T? Note that the current We_T is about 3 times the maximum We_P, so We_T and the smallest We_P are separated by about one order of magnitude.

4. The authors point out that the snapshot interval influences the physical interdependence of the measured events, and it is also known that the measured breakup statistics are sensitive to this interval due to algorithmic limitations. How may the authors decouple the two effects, especially in considering complex multi-scale events involving $m > 2$?

AUTHOR'S REPLY

We thank Dr. Chan for his questions, addressed below.

Question 1: Under weak entrainment τ_c is only a function of a_{max}, ε, and constants related to fragmentation statistics (Gaylo, *et al.*, 2021). Yu, *et al.* (2019) shows that turbulence near the free surface during entrainment is IHT. Thus, although we do not have active entrainment in our IHT simulations, the values we measure for these constants are directly applicable to entrainment-driven

fragmentation. To the second point, it is not immediately clear how the τ_c for entrainment-driven fragmentation we study here is related to the convergence timescales for pure fragmentation. However, the value of the entrainment-driven τ_c for identical fragmentation (Gaylo, *et al.*, 2021) is very similar to that found by Qi, *et al.* (2020) and Deike, *et al.* (2016) for pure fragmentation. Motivated by this apparent similarity, the authors intend on investigating the link between these two timescales in future work.

Question 2: This change in the shape of the daughter-size distribution would be reflected in a change in the value of $\tilde{C}_f$. The current study is restricted to $We_P > 39$, where we find that there is little variation in the daughter-size distribution with We_P (see figure 4), and thus $\tilde{C}_f$ a constant. We would expect some change in $\tilde{C}_f$ at smaller We_P where these Hinze-scale effects would become relevant.

Question 3: There are two ways to change the We_P of the parent bubbles we measure in simulations. The first is to change the size of the parent bubbles we measure relative to the domain (a_0/L) and the second is to change the turbulent Weber number (We_T) for the simulation. To ensure sufficient (and consistent) numerical resolution of daughter bubbles, we fix a_0/L, which fixes $a_0/\Delta x$ for a given resolution. Thus, to expand the range of We_P, the authors intend on running additional simulations at a wider range of We_T in future work.

Question 4: The dependence of fragmentation statistics on the snapshot interval Δt_s is a result of the definition of a fragmentation event being dependent on the (arbitrary) chosen value of Δt_s. In contrast, τ_c describes the time for a fragmentation cascade to reach an equilibrium, a definition with no inherent dependence on Δt_s. Therefore, we expect that, although each individual fragmentation statistics depends on Δt_s, C_τ should be independent of Δt_s. In future work, the authors will test this hypothesis by performing simulations using a range of Δt_s.

DISCUSSION

Prof. Rui Ni, Department of Mechanical Engineering, Johns Hopkins University.

This paper focuses on the bubble fragmentation in turbulence which is highly observable in the wake of surface vessels. By conducting DNS using the two-fluid cVOF method and ELA method, the authors are able to quantify in detail the bubble fragmentation process. Some important statistics are shown, including bubble number density, number of daughter bubble and daughter size distribution. Based on this information, the authors obtain the scaling constant of the critical time scale, which can be used to quantify the time period for the bubble to reach equilibrium state.

The paper shares some very exciting new development in this area. I just have some minor comments:

1. In equation 7, a constant C_f is defined based on number of daughters and daughter size distribution. It seems like this term can be used to quantify the difference among daughter PDFs. I wonder if the author could elaborate more on this constant in terms of the physical meaning.

2. Although the authors calculate C_Ω based on the data, it is still useful to show the curve of the breakup rate, which may be interesting to many readers.

3. In figure 4, the authors show the daughter size distribution. I would suggest that the authors could add experimental data to this figure. The data can be found in many of the references cited in this paper. At least qualitatively, the curves look reasonable. I won't expect adding experimental would weaken the point.

AUTHOR'S REPLY

We thank Professor Ni for his questions, addressed below.

Question 1: C_f is a measure of how dissimilarly-sized the daughter-bubbles are. For identical fragmentation (Valentas, *et al.*, 1966) where daughters are the same size, $C_f = 1$. For $\cap$-shaped distributions (e.g., Martínez-Bazán, *et al.* 1999b), the value of C_f is only slightly larger than 1 as many daughters are still similarly sized. The value of C_f increases for M-shaped (e.g., Martínez-Bazán, *et al.* 2010) and then further increases for $\cup$-shaped (e.g., Tsouris & Tavlarides 1994) as daughter bubbles are more likely to be dis-similarly sized.

Question 2: In figure 6 we provide the fragmentation rate $\Omega(a)$ as a function of We_P.

Question 3: We provided this comparison in figure 7. Our measurements of binary breakup provide daughter bubble-size distributions qualitatively similar to experiments (Hesketh, *et al.*, 1991; Rodríguez-Rodríguez, *et al.*, 2003; Vejražka, *et al.*, 2018; Qi, *et al.*, 2020).

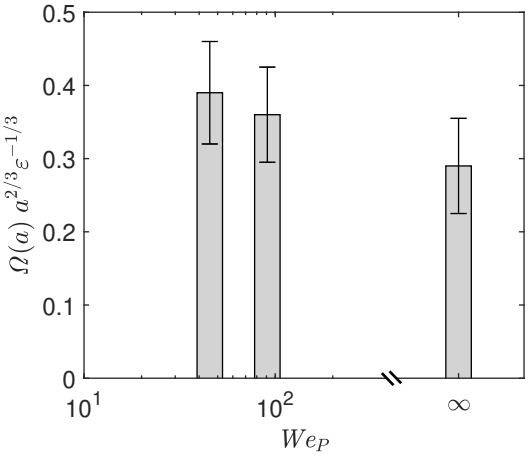

Figure 6: Measured fragmentation rate based on resolved fragmentation events. Error bars indicate 95% C.I.

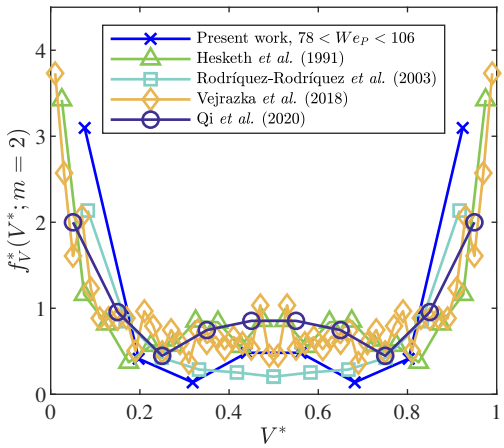

Figure 7: Non-dimensionalized volume-based, binary, daughter bubble-size p.d.f. compared to experimental data (as presented by Qi, *et al.* (2020, fig. 1)).